J. Fluid Mech. (1995), *vol.* 295, *pp.* 23–42

Nonlinear growth of the shock-accelerated instability of a thin fluid layer

By J. W. JACOBS[1], D. G. JENKINS[2], D. L. KLEIN[2] AND R. F. BENJAMIN[2]

[1] Department of Aerospace & Mechanical Engineering, University of Arizona, Tucson, AZ 85721, USA

[2] Los Alamos National Laboratory, Los Alamos, NM 87545, USA

(Received 15 October 1993 and in revised form 28 January 1995)

Richtmyer–Meshkov instability causes spatially periodic perturbations initially imposed on a shock-accelerated, thin gas layer to develop into one of three distinct flow patterns. Planar laser-induced fluorescence imaging of the evolving layer, produced by a perturbed SF_6 planar jet in air, shows an apparent flow bifurcation that is observed as mushroom-shaped or sinuous-shaped interfacial patterns. Analysis of this nonlinear instability growth, accomplished by modelling the flow field as a row of line vortices, predicts that the layer thickness grows logarithmically at later times and compares well with our measurements. Because the row of vortices is unstable, the model also provides an explanation for the appearance of the three observed interfacial patterns.

1. Introduction

The instability of an accelerated interface between fluids of different densities is a fundamental problem in fluid mechanics. Richtmyer–Meshkov (R–M) instability occurs at a perturbed planar interface subjected to impulsive acceleration, such as caused by the interaction of a shock wave propagating from a lower-density fluid into higher-density fluid, or vice versa (Richtmyer 1960; Meshkov 1969; PCTM Workshops 1988–93 including, for example, Benjamin 1988). It has similarities to the well-known Rayleigh–Taylor (R–T) instability of an interface which is driven by constant acceleration, such as gravity (Rayleigh 1900; Taylor 1950; Lewis 1950; Sharp 1984). The nonlinear growth of R–M or R–T instability of a single interface produces complex flow structures, but when R–M instability occurs at nearby interfaces, the coupling between interfaces appears to produce additional complexities including an apparent flow bifurcation. We observed this previously unreported bifurcation in shock-tube experiments involving the shock acceleration of a thin fluid layer of SF_6 gas imbedded in air (Jacobs *et al.* 1993). This discovery resulted from applying the combination of two innovative experimental techniques (Jacobs 1992, 1993): (i) forming the initial rippled planar interfaces with a laminar gas jet without the use of membranes, and (ii) observing the flow with planar laser-induced fluorescence (PLIF) imaging.

Flows evolving from R–M unstable interfaces are of practical interest in applications including inertial confinement fusion, projectile acceleration, combustion, and astrophysics (Shaner 1984). For example, the pusher shell in an ICF direct-drive target is a high-density layer between two lower-density layers, the ablation layer on the outside and the fuel within. The ablation/pusher/fuel interfaces are susceptible to R–T

and/or R–M instabilities, depending on the acceleration history during the implosion (McCall 1983). Another application is the rapid acceleration of a thin projectile by a gaseous propellant. Knowledge of the instability growth of a thin layer is vital for designing better interfaces for these and related applications. It is also useful for interpreting past experiments, and developing fluid simulations to predict interfacial mixing more accurately.

While experiments using liquid/liquid interfaces have successfully measured R–M growth (Benjamin & Fritz 1987), previous R–M experiments in gas/gas systems have had difficulty both in forming fluid interfaces and in visualizing the flow. Forming a massless, discontinuous interface between two gases is difficult. Meshkov (1969) and others (PCTM Workshops 1988–93; Benjamin, Besnard & Haas, 1993; Andronov *et al.* 1976; 1983; Brouillette 1989) have performed shock-tube experiments using a membrane to separate two gases, initially at the same pressure but having different densities. however, the influence of the membrane on the resulting flow evolution in these experiments is believed to be significant and is difficult to assess, making comparison with other experimental and computational investigations troublesome. Shock-tube experiments designed to avoid membrane effects have used gravitational stratification (Brouillette 1989; Cavaillier *et al.* 1990) to produce membrane-less but diffuse interfaces, typically having initial diffusion regions about 1 cm thick. However, the diffuse interfaces tend to stabilize all but the longest wavelengths, greatly reducing the resulting instability growth rate. This significantly lengthens the time required to observe a substantial growth in amplitude. In addition, it increases the unwanted influence of shock-tube boundary layers on the flow, and inhibits the generation of turbulence. Flow visualization used in most previous experiments has been schlieren or shadowgraphy. These methods spatially integrate along the line of sight and suffer severely from optical distortion induced by boundary effects which badly obscure the free-stream flow. Radiography (Bonazza 1992) is less sensitive to wall effects, and provides quantitative data on the interfluid mixing induced by R–M instability. However, it also spatially integrates the profile and is therefore of limited use in visualizing the interfacial profile. Our experiments overcome the difficulty of creating the initial interface by utilizing a laminar gas jet to produce a 'gas curtain', which avoids the problems of membranes and stratified layers. In addition, we eliminate the visualization problem by using planar laser-induced fluorescence (PLIF) imaging which measures a two-dimensional cross-section of the flow, unobscured by boundary effects.

The early stage of the R–M instability is described by linear perturbation theory (Richtmyer 1960), which shows that an initial perturbation will grow in amplitude at a constant rate following transients imposed by shock acceleration. The constant growth rate may also be estimated from an impulse model (Richtmyer 1960; Mikaelian 1990) based on Taylor's (1950) analysis of the R–T problem. Recent studies (Yang, Zhang & Sharp, 1993) describe the precise relationship between the linear theory and impulse model. When the amplitude becomes comparable with the perturbation wavelength, nonlinear effects including saturation, mode-coupling and secondary instabilities dominate this 'nonlinear regime'. Visually, the intermediate stage of the instability of a single interface with large density ratio is observed as spike and bubble patterns, where the spikes of higher-density fluid protrude into lower-density fluid. For a density ratio of nearly one, the interface evolves into a pattern in which fluid interpenetration is symmetric; the shapes of the higher-density and lower-density penetrating regions are visually similar. The late stages of R–T growth are well modelled by the self-similarity formulation of Youngs (1984) and the renormalization

theory of Glimm, Sharp & Zhang (1991). However, the difficulty in solving the nonlinear governing equations precludes analytic solutions for the intermediate, nonlinear stage of the R–M instability and its transition into turbulence. We develop a simple model aimed at describing the nonlinear instability growth by considering the production and transport of vorticity. This model is consistent with our experimental observations, and agrees well with our measurements of layer growth.

This paper describes our experiments with emphasis on the benefits of the gas curtain and PLIF (§2). Observations of the three flow patterns and measurements of the layer thickness are presented in §3. The instability growth is then analyzed in §4, using linear perturbation theory combined with a model based on the dynamics of a linear array of vortices.

2. Experimental technique

We utilized experimental techniques similar to those used by Jacobs (1992) in which planar laser-induced fluorescence (PLIF) was used to visualize the flow of shock-accelerated cylindrical jets. As mentioned above, using a laminar flow to produce a density interface improves on previous experiments which utilized thin membranes to separate the gases. In these experiments, pieces of membrane broken by the shock impact both disturbed flow development and impaired visualization. In addition, PLIF imaging allowed for the acquisition of a cross-sectional view of the nearly two-dimensional flow without the obscuring effects of boundary disturbances and slight three-dimensionality. Multiframe schlieren imaging was first attempted in this study but was abandoned because of these detrimental effects (as will be described later).

A 4 m long horizontal shock tube with a 75 mm square cross-section (shown schematically in figure 1) was used to impulsively accelerate a vertical, nearly planar jet of SF_6. Mach 1.2 shock waves were produced by the mechanical puncture of Mylar diaphragms which initially separated the driver section (pressurized to 103 kPa above ambient) from the driven section (initially at ambient conditions) of the shock tube. Three He–Ne laser timing detectors measured shock speed immediately upstream of the initial SF_6 layer and triggered flow diagnostics. The test section had schlieren-grade windows above and below the portions of the shock tube immediately upstream and downstream of the nozzle.

A nearly planar jet, flowing from a contoured nozzle at the top of the viewing test section, produced the SF_6 layer. Spatially modulating the jet in the horizontal direction created initial perturbations. A nearly two-dimensional varicose profile was generated by the inlet nozzle shape shown in figure 2, which is a series of 4.76 mm holes with 5.95 mm spacing connected by a 2.38 mm slot. A 9.52 mm outlet slot placed opposite the inlet at the bottom of the test section removed the SF_6 along with some air to prevent contamination of the shock tube. SF_6 was supplied at a rate of 3.3 l min^{-1} and exhausted at 10 l min^{-1}. Because exit flow was greater than entering flow, air was allowed to enter the shock tube upstream and downstream of the test section. Contamination of the shock tube was further minimized by firing a shock soon (approximately 10 s) after starting the gas flow. We found this to be the minimum time needed to stabilize the jet. The vertical speed of the initial jet (approximately 0.2 m s^{-1}) was considerably less than the relative flow velocities generated by the shock interaction (approximately 20 m^{-1} s). Thus, the jet flow was inconsequential to the flow produced by the shock wave. A schlieren system which passed diagonally across the test section monitored the initial flow for stability. The jet was always observed to be laminar, although a very small amount of unsteadiness was often apparent.

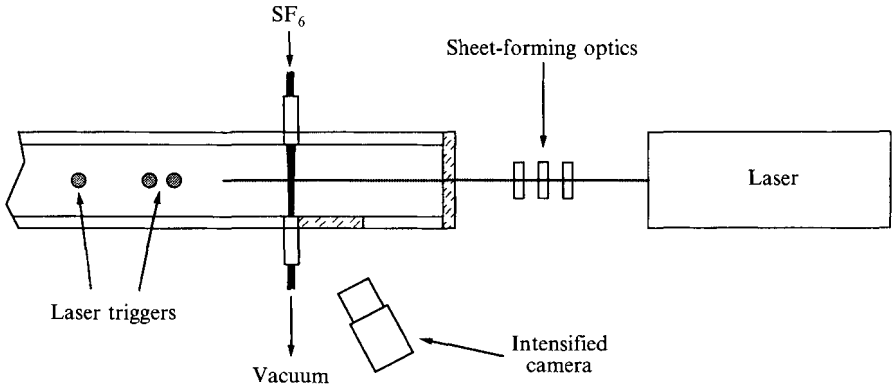

FIGURE 1. Schematic of the experimental apparatus, shown not to scale. The shock tube has a 75 mm square inside cross-section.

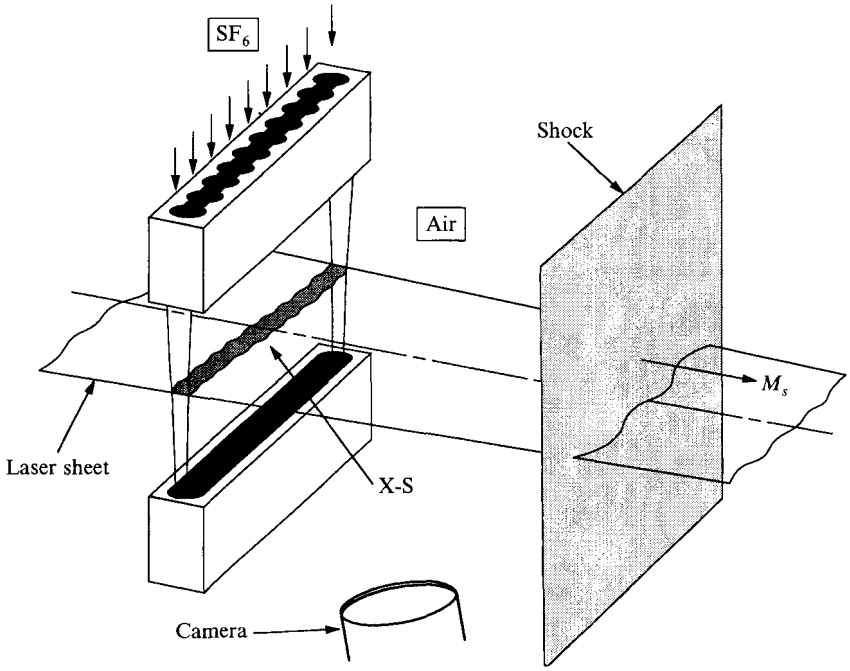

FIGURE 2. The perturbed, thin layer of SF_6/diacetyl flows downward in the shock-tube test section from a plenum/nozzle assembly atop, through the test section, and into an exhaust vent below. The PLIF probe is a horizontal laser sheet that intersects the thin layer at the illuminated cross-section, denoted X-S, which the intensified CCD camera views. The incident shock accelerates the layer from left to right, and the observed profiles are displaced downstream from the initial position depicted in this diagram. The profile of the flow seen in the X-S region is smoothed relative to the nozzle profile, but the dominant perturbation wavelength (6 mm) remains the same. This schematic diagram is shown not to scale.

The PLIF flow visualization system (shown in figure 1) used a flashlamp pumped dye laser (Candela LFDL-8 using Coumarin 120 dye) with its output tuned to 440 nm, producing a 200 mJ, 10 μs pulse. The laser beam entered the shock tube through a transparent endwall. Cylindrical lenses spread the beam horizontally to a width of 4 cm, while focusing it vertically to 2 mm to form a laser sheet inside the test section. The laser sheet illuminated a cross-section of the SF_6 layer which was seeded with one part

diacetyl vapour per hundred parts SF_6. Diacetyl is a fluorescent dye which absorbs light at 420–450 nm, and fluoresces with a peak at 470 nm (Epstein 1974). A gated, intensified CCD camera (Cohu 4815 with LANL intensifier) captured the resulting fluorescent image through a window in the bottom of the test section. A frame grabber (EPIX) and camera synchronization support card (Big Sky Software) installed in a microcomputer (IBM PC/AT) captured and digitized the image. A 5 μs gate length on the camera was used to reduce image blurring caused by the layer's movement during capture, and long-pass filters (Schott Glass GG455) blocked the original laser light so that only fluorescent light was recorded by the camera. One frame of the moving flow was captured per event. In addition, initial conditions were recorded 1 s before shock arrival, whenever both initial conditions and shock-accelerated flow were within the camera's view. The laser's maximum repetition rate (approximately 4 Hz) was too slow to allow the recording of both initial conditions at shock impact and subsequent flow.

Diacetyl was used in these experiments as a tracer to track the location of SF_6, but because SF_6 and diacetyl diffuse at different rates, the effectiveness of diacetyl as a tracer is arguable. However, good comparison between recent experiments using Rayleigh scattering (Budzinski 1992, see also the preliminary account in Budzinski, Zukoski & Marble 1992) and similar experiments utilizing diacetyl (Jacobs 1992), demonstrate the effectiveness of diacetyl as a tracer gas for SF_6 in these types of experiments.

3. Observations

We observed three flow patterns, described in detail below and pictured in figures 3–5, by visually creating ensembles of images from approximately 100 PLIF images. Although the patterns in figures 3–5 are displayed as sequences of images, each image corresponds to a different experimental event. Adjusting the trigger delay to the laser/camera system controlled the time of each image. Thus, visual judgement determined the classification of each image.

The three instability modes appear to be randomly occurring in that we could neither predict nor control which mode would appear during a particular experiment. Repeated observations at the same time and location after shock impact showed different modes. Approximately 50% of the images can be assembled into a sequence represented by figure 3, denoted 'upstream mushrooms'. In this sequence the perturbed layer forms a series of mushroom-shaped features oriented opposite to the shock direction (i.e. upstream). However, about 10% of the images can be assembled into sequences like that in figure 4, in which the flow forms mushrooms oriented in the shock direction (downstream). The remaining 40% of the PLIF images form a sequence such as depicted in figure 5, in which the flow forms a sinuous shape devoid of vortex formation until late in the evolution process (i.e. about 1 ms after shock interaction). No PLIF image taken at a time less than 1 ms after shock interaction exhibits more than one type of disturbance.

The three modes of instability evolve from nearly identical initial conditions. The jet technique produces predominantly two-dimensional SF_6 layers modulated with a varicose perturbation. Figure 6 depicts several PLIF cross-sections of the initial layer (actually this is a time sequence having a 1 s interframe time). Small variations in initial layer shape are apparent in these images. These variations occur because the jet was not completely steady. As mentioned above, we observed a small degree of unsteadiness when monitoring the initial flow with our initial-condition monitoring schlieren

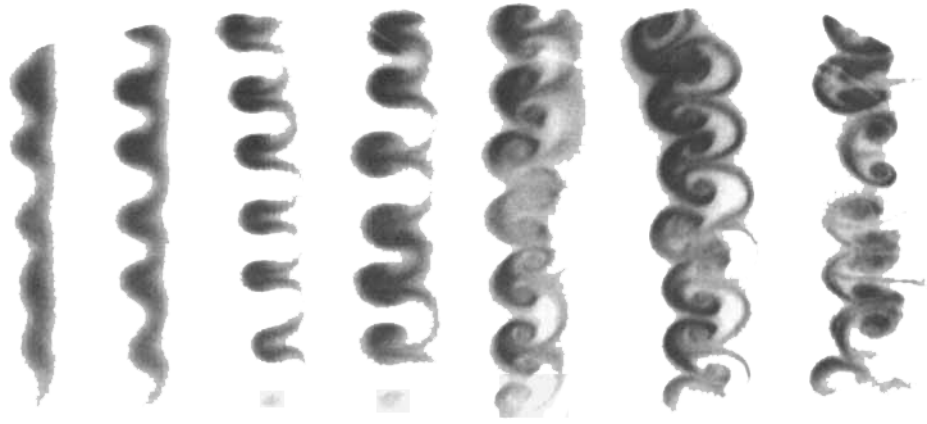

FIGURE 3. This time sequence of PLIF images shows clearly one of the three distinct profiles that evolve from nearly identical initial conditions. The shock wave has passed from left to right. The distance between successive images in the figure does not represent the actual displacement of the layer in the shock tube. Because each image is taken on a different event, detailed features do not register frame-to-frame. However, the dominant growth features are reproducible. These 'upstream mushrooms' have the mushroom caps oriented opposite to the direction of shock-wave motion. Darker regions indicate stronger fluorescent emission and therefore higher concentration of SF_6/diacetyl. The time of each frame after shock impact with the layer is: (*a*) 137 μs, (*b*) 241 μs, (*c*) 339 μs, (*d*) 440 μs, (*e*) 582 μs, (*f*) 741 μs, (*g*) 937 μs.

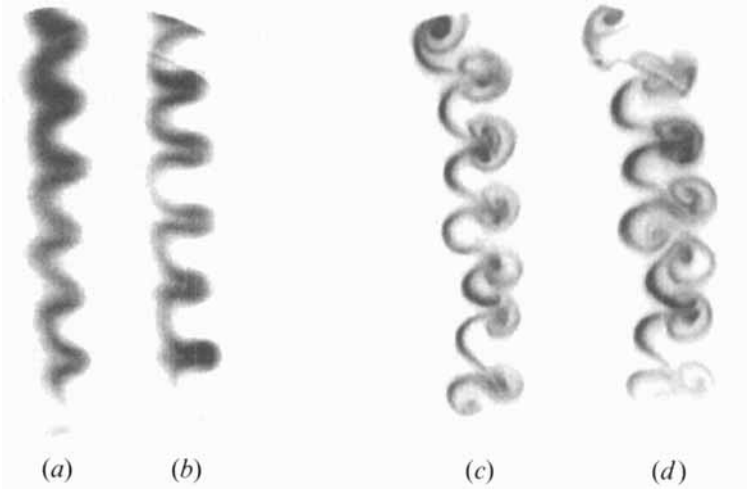

FIGURE 4. The 'downstream mushrooms' are similar to the upstream mushrooms of figure 3 but oppositely directed. They occur rarely in our experiments. Like upstream mushrooms, they appear to be driven by vortex pairs and produce mixing by entraining the ambient air within the SF_6 test gas. The time of each frame after shock impact with the layer is: (*a*) 241 μs, (*b*) 396 μs, (*c*) 744 μs, (*d*) 893 μs.

system. Thus, although our technique produced a largely reproducible initial flow, small uncontrollable variations in the initial layer shape were also present. We believe that the small differences in the initial shape produce the large differences observed in subsequent flows, as shown in figure 3–5. As mentioned earlier, the speed of the initial

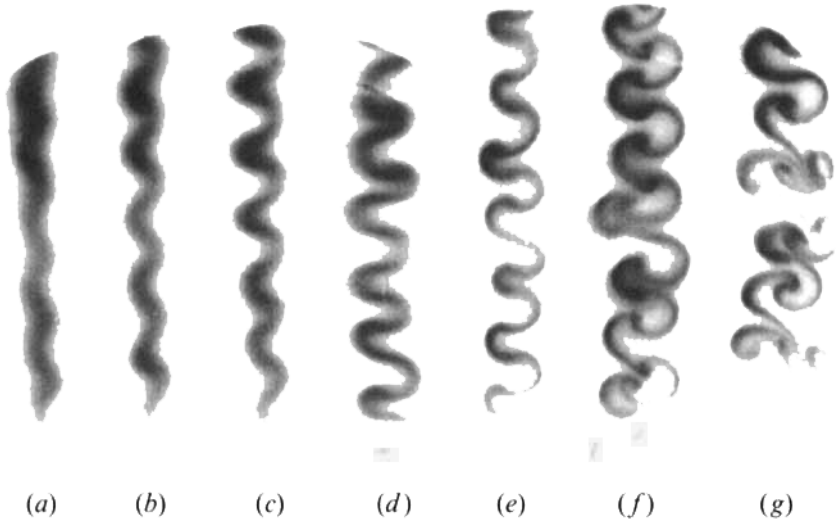

FIGURE 5. Sinuous evolutions appear to lack vortices until late times, and thereby mix the gases less effectively than mushroom profiles. The time of each frame after shock impact with the layer is: (*a*) 148 μs, (*b*) 194 μs, (*c*) 238 μs, (*d*) 438 μs, (*e*) 537 μs, (*f*) 790 μs, (*g*) 942 μs.

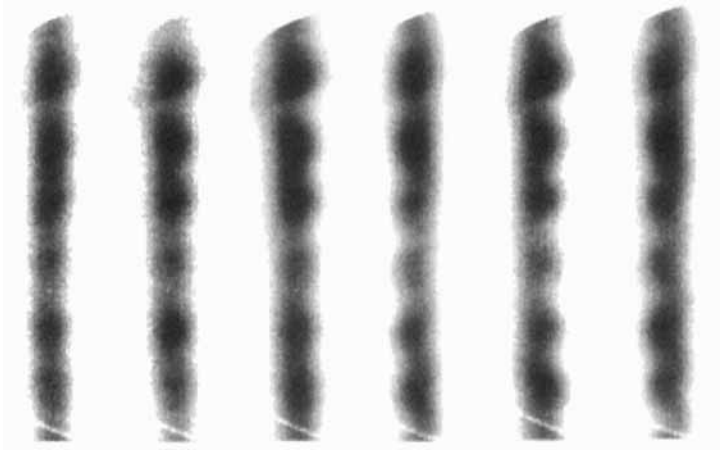

FIGURE 6. PLIF images of initial SF_6 layer revealing the small variations in shape. This is a time sequence having a 1 s interframe time.

jet flow is much less than the post-shock flow, so we expect the initial velocity field to be unimportant.

Immediately after shock passage the three modes of instability evolve similarly. The perturbations on the upstream surfaces grow while the downstream perturbations invert phase and then grow, changing the initial varicose layer profile into a thinner sinuous one. In the sequence depicted in figure 3, the upstream edge of the layer initially grows at a faster rate than the downstream edge, producing cusps oriented in the upstream direction which are reminiscent of the bubble and spike patterns observed in single-interface R–T and R–M instabilities. In figure 4 the layer evolves similarly to figure 3 but in the opposite direction, producing cusps facing downstream. The location of the cusps in figure 4 corresponds to the thin region of the initial layer. Thus they are 180° out of phase from the sequence shown in figure 3. In the sinuous sequence

FIGURE 7. PLIF image taken with the laser sheet thickness increased from 0.2 to 2.7 cm in order to demonstrate the two-dimensionality of the flow.

(figure 5) the boundaries grow at comparable rates, thus retaining the symmetry of the sinuous shape.

The cusps of figure 3 further evolve into lobes, eventually forming vortex pairs which propagate upstream, against the flow in the shock tube. Similarly, more slowly growing vortex pairs develop in figure 4 which travel in the opposite direction. Note that the downstream-facing mushrooms develop in regions having significantly less SF_6 than the upstream mushrooms. Thus the downstream-propagating vortex pairs entrain noticeable amounts of air. In figure 5 the sinuous mode grows symmetrically without the appearance of vortices.

The three modes develop into turbulent flow in slightly different ways. Late in the process the upstream mushrooms have grown to a point where they begin to interact with neighbouring vortex pairs creating a more turbulent flow. The downstream mushrooms interact at a later time because of their delayed growth. In the late stages of the sinuous sequence vortices also begin to appear randomly during its transition into a turbulent flow. The Reynolds number of the flow can be estimated using the perturbation wavelength (≈ 6 mm) as a length scale, the instability growth rate (≈ 15 m s^{-1}) as a velocity scale, and either the viscosity of air (0.15 cm^2 s^{-1}) or SF_6 (0.025 cm^2 s^{-1}), yielding $Re(\nu_{air}) = 6000$ and $Re(\nu_{SF_6}) = 36000$.

Through the layer's early to intermediate time of development, the flow remains predominantly two-dimensional. This is shown in figure 7, where the thickness of the laser sheet was expanded to 2.7 cm, while the flow was observed at an angle nearly perpendicular to the sheet. Vertical variance is apparent; however, the length scale of this variation is significantly longer than that of the predominantly two-dimensional features. Furthermore, the vortex formation and pairing, which governs flow development, appears to be nearly uniform along the vertical axis.

Figure 8 is a sequence of schlieren images of the evolving layer taken from a similar perspective as the PLIF images described above. Notice that although there is strong evidence of a developing periodic structure in the layer, there is no indication of the mushroom or sinuous shapes observed in the PLIF images. In addition, in the schlieren

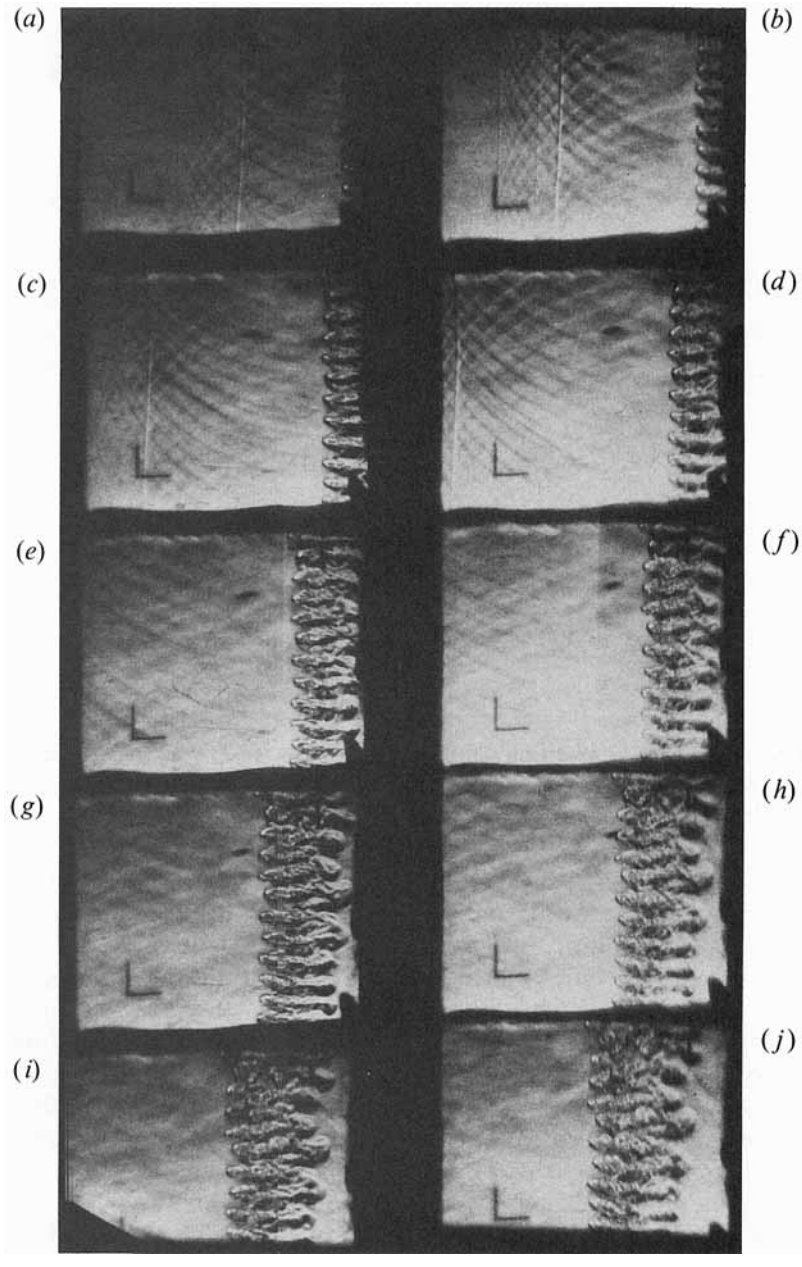

FIGURE 8. Multiframe schlieren image of the evolving layer which shows periodic structure, but no indication of the patterns observed in figures 3–5. Flow is from right to left. Interframe time is 40 μs.

view the layer appears to be significantly thicker (perhaps by an order of magnitude) than it evidently is, as observed in the PLIF images. These differences are probably due to edge effects near the shock-tube windows obscuring the flow. In addition, a slight tilting of the layer similar to that which occurs with shock-accelerated cylinders (Jacobs 1992, 1993) could also cause the schlieren-viewed layer to appear much thicker than it really is.

The accelerated gas layer is pushed downstream by the flow behind the shock wave.

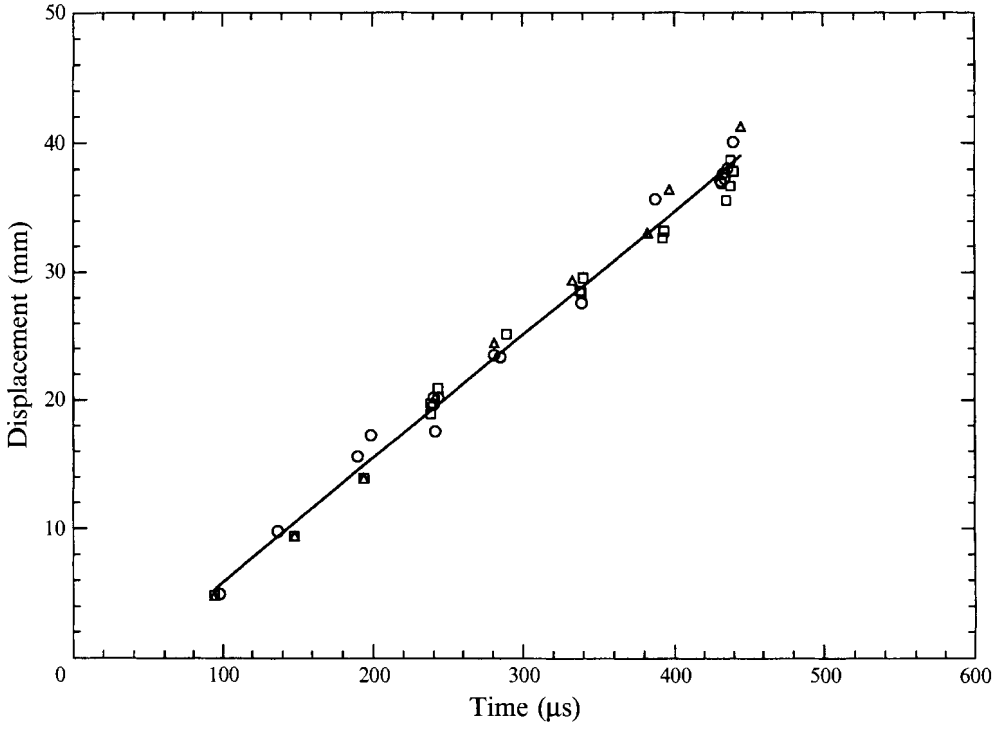

FIGURE 9. Plot of the mean downstream displacement of the layer. The line is a linear curve fit of the data yielding a translational velocity of 96 m s^{-1}. ○, Upstream mushroom pattern; △, downstream mushroom pattern; □, sinuous pattern.

This is observed in figure 9 which shows the mean downstream displacement of the layer (found by averaging the mean displacement of the downstream peaks with those of the upstream peaks), plotted versus the time interval from predicted shock impact. notice that these early time data fall on a straight line, indicating a constant translational velocity of 96 m s^{-1}. This is slightly less than the piston velocity (as calculated from the shock speed, assuming a completely air-filled shock tube, $= 106 \pm 2$ m s^{-1}). Also note that the trajectory line does not pass through the origin, indicating that the time at which the constant translational velocity is initiated (i.e. the time of the impulsive acceleration) differs from the predicted shock impact time by approximately 39 μs. This difference may partly be due to error in the prediction of the shock impact time caused by the incomplete removal of SF_6 from the shock tube. Note that if the jet fluid was not completely removed, the air upstream of the jet would probably be contaminated with SF_6. This would produce a slightly lower shock speed in that region, and thus a slight delay in the shock arrival time. However, the offset in figure 9 is more likely an indication of the finite time required to accelerate the layer. The layer is not accelerated to its final velocity immediately upon shock impact. The acceleration process occurs over a short, but finite, period of time during which the incident shock wave and generated reflected waves reverberate through the layer. This process occurs over many reflections. However, because the strengths of the reverberating waves decay quickly, the acceleration time can be reasonably estimated by the time it takes the incident shock wave to travel across the layer and reflect back as an expansion. A one-dimensional calculation of this process yields 17 μs for the transit of the initial shock wave through the layer, and an additional 15 μs for the transit of the reflected

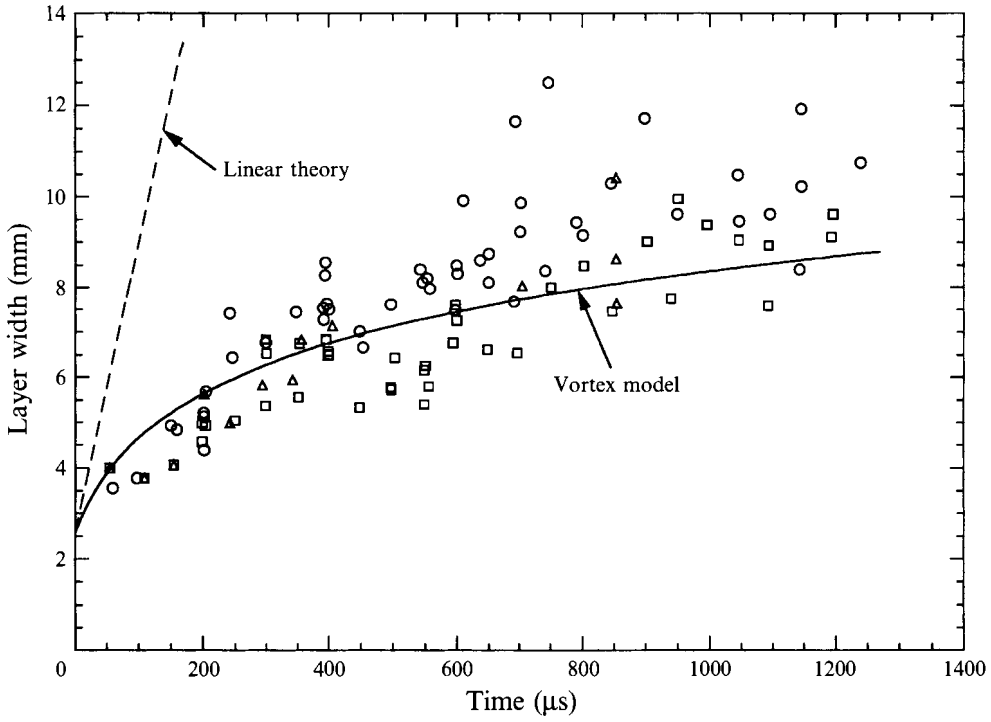

FIGURE 10. Plot of the growth in thickness of the layer. The curve marked 'Vortex model' is obtained using equation (36), and 'Linear theory' corresponds to equation (39), both evaluated with estimates of the experimental parameters. ○, Upstream mushroom pattern; △, downstream mushroom pattern; □, sinuous pattern.

expansion wave back through the compressed layer. This gives a total of 32 μs as an approximation for the time necessary to accelerate the layer, which agrees well with the measured offset in figure 9.

Figure 10 shows the growth of the width of the perturbed layer, defined as the average distance between its leading and trailing edges. Note that the time scale in this plot is corrected by the measured time offset found from figure 9. There is significant scatter in the data; however, the layer width measured from runs showing upstream mushroom behaviour appears to grow significantly faster than those exhibiting the other patterns. The error in these measurements is estimated to be less than the symbol size used. Therefore, the observed scatter in this plot is probably the result of the small differences in the initial conditions (as described above) that also produce the large differences we observe as different patterns. The time behaviour of layer thickness shows little (if any) of the linear growth stage normally expected for early-time R–M instability. This is not surprising considering that the initial amplitude of the perturbations in our experiments is comparable to the wavelength. The shape of the observed growth curve suggests that nonlinearity has a strong influence during the middle to late stages of our observations.

4. Interpretation and analysis

The development of the observed patterns shown in figures 3–5, particularly the dominance of the vortices in these images, suggests that vortex dynamics may be utilized to model the intermediate and late time instability. Vorticity is initially

deposited in the layer by the misalignment of pressure and density gradients which occurs during the shock interaction and eventually evolves into vortices. In this section we develop a model, based on the dynamics of a row of vortices, which describes the intermediate and late time behaviour of a shock-accelerated thin fluid layer. The model is heuristic, and therefore intended only to provide insight into the flow physics and to estimate the growth of the layer width. Because the strength of these vortices is determined during the shock interaction, we must first look at the initial stages of the instability, in order to obtain estimates of these strengths.

The interaction process is a complicated one. The incident shock wave first impacts the upstream interface, generating vorticity on that boundary as it passes through it. This interaction produces a reflected wave (a shock) which travels back upstream and a transmitted wave (another shock) which continues to travel downstream and impact the second interface. This second interaction generates reflected and transmitted waves (reflected expansion and transmitted shock) and additional vorticity. At this point the incident shock wave has passed through the layer, but the interaction process is not yet complete. The expansion wave generated by the interaction of the incident shock with the downstream interface travels back upstream and impacts the upstream interface, depositing additional vorticity on that interface. Part of this wave is then reflected again to further modify the vorticity on the downstream interface, and so on. Therefore, the interaction of a shock wave with the layer generates a succession of reverberating waves. Furthermore, an accurate estimate of the circulation deposited by this interaction must include the effects of these waves.

Richtmyer's (1960) impulse model, although simplistic, is well suited to estimate the vorticity generated during the entire interaction process. The model assumes incompressible flow and approximates the series of interactions as impulsive accelerations, and thus uses the final layer velocity as the input parameter which specifies the total impulse strength. This model is an obvious simplification of what is in reality a very complex interaction process. However, it has been shown to provide good accuracy when compared with results from shock-tube experiments. In contrast, an analysis based on correctly modelling only a single interaction of the shock wave with each interface, more accurately predicts the vorticity generated by this single interaction, but cannot accurately predict the final vorticity distribution because it does not model the entire interaction process.

4.1. *Instability of an impulsively accelerated layer*

Following the analysis of Richtmyer (1960) we assume that the early time behaviour of the shock-accelerated layer (providing that the initial amplitude is sufficiently small) may be suitably described by the linear instability of an impulsively accelerated fluid layer. Let us first consider a system of two incompressible and initially irrotational fluids of density ρ_1 and ρ_2, and velocity potentials ϕ_1 and ϕ_2 (where $\boldsymbol{v} = \nabla\phi$), separated by a nearly planar interface with perturbation η (figure 11 *a*). The equations which govern the growth of infinitesimal disturbances on the boundaries of the layer are

$$\nabla^2\phi = 0 \tag{1}$$

in each of the two fluids, with

$$\frac{\partial\eta}{\partial t} - \frac{\partial\phi}{\partial y} = 0, \tag{2}$$

$$\rho\frac{\partial\phi}{\partial t} - \rho g\eta + p = P_0 \tag{3}$$

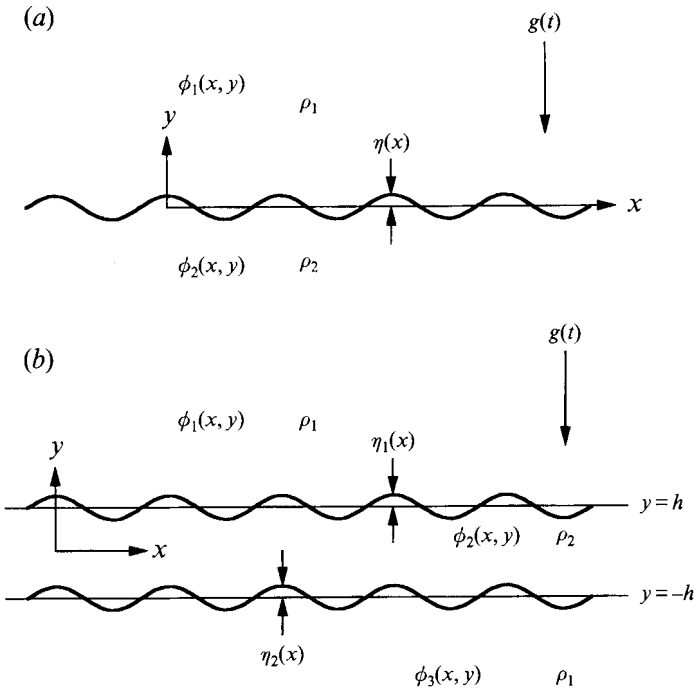

FIGURE 11. Schematic showing the configuration analysed using linear stability theory for (*a*) single, and (*b*) double interface systems.

on $y = 0$, where p is pressure, g is the acceleration, and P_0 is a constant, equal to the pressure at the interface in the unperturbed rest state. A periodic perturbation on the interface of the form

$$\eta = a(t)\cos kx \tag{4}$$

then requires the following velocity potentials in the two fluids:

$$\phi_1 = b(t)\,\mathrm{e}^{-ky}\cos kx, \quad \phi_2 = -b(t)\,\mathrm{e}^{ky}\cos kx, \tag{5}$$

which when substituted into the interfacial conditions (2) and (3) yield

$$\mathrm{d}a/\mathrm{d}t = -kb, \tag{6}$$

$$\mathrm{d}b/\mathrm{d}t = -Aga, \tag{7}$$

where

$$A = (\rho_2 - \rho_1)/(\rho_2 + \rho_1) \tag{8}$$

is the Atwood number.

Equations (6)–(8) can be combined to yield an ordinary differential equation for $a(t)$:

$$\mathrm{d}^2a/\mathrm{d}t^2 = kAga. \tag{9}$$

For R–M instability, the acceleration g can be written as the product of a velocity jump and a Dirac delta function (i.e. $g = \Delta V\delta(t)$) allowing (9) to be easily integrated. Thus,

$$\mathrm{d}a/\mathrm{d}t = kA\,\Delta V a_0, \tag{10}$$

where ΔV is the velocity change induced by the impulsive acceleration and a_0 is the amplitude of the initial perturbation. Notice that a disturbance on a light–heavy interface (thus having positive Atwood number) will grow linearly with time, while one

on a heavy–light interface (having negative Atwood number) will invert phase before growing.

Now consider a planar fluid layer with thickness $2h$ and density ρ_2 surrounded by fluid of density ρ_1 (figure 11*b*). Equation (1) still applies in each of the two fluids with (2) and (3) now applied on $y = \pm h$. Periodic perturbations on each of the two interfaces of the form

$$\eta_1 = a_1(t)\cos kx, \quad \eta_2 = a_2(t)\cos kx \tag{11}$$

now require the following velocity potentials:

$$\left.\begin{aligned} \phi_1 &= b_1(t)\,\mathrm{e}^{-k(y-h)}\cos kx, \\ \phi_2 &= -\left(\frac{b_1+b_2}{2}\frac{\sinh ky}{\cosh kh}+\frac{b_1-b_2}{2}\frac{\cosh ky}{\sinh kh}\right)\cos kx, \\ \phi_3 &= -b_2(t)\,\mathrm{e}^{k(y+h)}\cos kx, \end{aligned}\right\} \tag{12}$$

which when substituted into the interfacial conditions, (2) and (3), yield

$$\mathrm{d}a_1/\mathrm{d}t = -kb_1, \tag{13}$$

$$\mathrm{d}a_2/\mathrm{d}t = -kb_2, \tag{14}$$

$$\mathrm{d}b_1/\mathrm{d}t + \mathrm{d}b_2/\mathrm{d}t = -A_t g(a_1-a_2), \tag{15}$$

$$\mathrm{d}b_1/\mathrm{d}t - \mathrm{d}b_2/\mathrm{d}t = -A_c g(a_1+a_2), \tag{16}$$

where

$$A_t = \frac{\rho_2-\rho_1}{\rho_2\tanh kh+\rho_1}, \tag{17}$$

$$A_c = \frac{\rho_2-\rho_1}{\rho_2\coth kh+\rho_1} \tag{18}$$

define two new modified Atwood numbers. Note that in the limit of a very thick layer (i.e. $kh\to\infty$) $A_t = A_c = A$. Equations (13)–(16) can be combined to yield a pair of ordinary differential equations for a_1 and a_2:

$$\mathrm{d}^2a_1/\mathrm{d}t^2 + \mathrm{d}^2a_2/\mathrm{d}t^2 = kA_t g(a_1-a_2), \tag{19}$$

$$\mathrm{d}^2a_1/\mathrm{d}t^2 - \mathrm{d}^2a_2/\mathrm{d}t^2 = kA_c g(a_1+a_2). \tag{20}$$

Equations (19) and (20) are consistent with Taylor's (1950) result in which he considered the instability of a thin liquid layer (i.e. $\rho_1 = 0$) under constant acceleration. Again writing the acceleration g as the product of velocity jump and a Dirac delta function allows for the easy integration of (19) and (20). Thus,

$$\mathrm{d}a_1/\mathrm{d}t + \mathrm{d}a_2/\mathrm{d}t = kA_t\Delta V(a_{1,0}-a_{2,0}), \tag{21}$$

$$\mathrm{d}a_1/\mathrm{d}t - \mathrm{d}a_2/\mathrm{d}t = kA_c\Delta V(a_{1,0}+a_{2,0}). \tag{22}$$

Using a δ-function to model the shock interaction with the thin heavy-gas layer assumes that the layer is sufficiently thin so that the time difference between shock impact of the two surfaces is negligible. Notice that for a varicose type of initial perturbation, $a_{2,0} = -a_{1,0} \equiv -a_0$, so

$$\mathrm{d}a_1/\mathrm{d}t = \mathrm{d}a_2/\mathrm{d}t = kA_t\Delta V a_0. \tag{23}$$

Similarly for a sinuous type perturbation, $a_{2,0} = a_{1,0} \equiv a_0$, and

$$\mathrm{d}a_1/\mathrm{d}t = -\mathrm{d}a_2/\mathrm{d}t = kA_c\Delta V a_0. \tag{24}$$

Just as occurs in linear R–M theory for a single interface, a disturbance on the light–heavy interface (i.e. the upstream interface in the experiments) will grow linearly with time, and a disturbance on the heavy–light interface (i.e. the downstream interface in the experiments) inverts phase and then grows. Thus, an initially varicose-shaped layer should evolve into a sinuous shape and an initially sinuous shape should evolve into a varicose one.

Equations (23) and (24) differ from the equivalent expression obtained for a single interface (equation (10)) in that the modified Atwood numbers A_t and A_c depend on the layer thickness. However, as mentioned earlier, when the layer thickness approaches infinity A_t and A_c approach the standard definition of the Atwood number. Thus for sufficiently large values of kh the two interfaces act independently. It is interesting to note that as the layer thickness approaches zero, $A_t \to (\rho_2 - \rho_1)/\rho_1$ and $A_c \to 0$. Thus, growth is enhanced for a varicose disturbance on a heavy layer and inhibited for a varicose light layer. But for a sinuous layer, growth is always inhibited and is zero in the limit of an infinitesimally thin layer.

4.2. *Vortex-dominated instability growth*

A characteristic of the fluorescent images of figures 3–5 is the obvious development of vortices and their dominant role in the fluid flow. The importance of vorticity in the development of shock-induced flows is well known (Picone & Boris 1988; Hawley & Zabusky 1989; Yang, Zabusky & Chern 1990). Vorticity is generated during the shock interaction process by the misalignment of pressure and density gradients as governed by the two-dimensional vorticity equation,

$$\rho \frac{\mathrm{D}}{\mathrm{D}t}\left(\frac{\boldsymbol{\omega}}{\rho}\right) = \frac{1}{\rho^2}\boldsymbol{\nabla}\rho \times \boldsymbol{\nabla} p, \tag{25}$$

where $\boldsymbol{\omega}$ is the vorticity vector, which is aligned normal to the plane of motion. The term on the right-hand side of (25) describes the production of vorticity, so vorticity is generated at a rate proportional to the cross-product of the pressure and density gradients. In the experiments the dominant pressure gradient is produced by the plane shock wave, and the dominant density gradient is at the boundary of the heavy-gas layer (as shown in figure 12*a*). Thus, the vorticity generated by this interaction will lie on the boundaries of the layer, and will vary periodically along its length.

In the model used in the linear stability theory described above, the boundary separating the two fluids is sharp, so the vorticity is concentrated in a thin sheet on the boundary. The strength of this sheet, γ, is equal to the jump in tangential velocity across each of the two boundaries. Thus, within the approximations of the linear analysis

$$\gamma_1 = \left.\frac{\partial \phi_2}{\partial x}\right|_{y=h} - \left.\frac{\partial \phi_1}{\partial x}\right|_{y=h}, \quad \gamma_2 = \left.\frac{\partial \phi_3}{\partial x}\right|_{y=-h} - \left.\frac{\partial \phi_2}{\partial x}\right|_{y=-h}, \tag{26}$$

$$\left.\begin{aligned} \gamma_1 &= -[A_t \tfrac{1}{2}(1+\tanh kh)(a_{1,0}-a_{2,0}) + A_c \tfrac{1}{2}(1+\coth kh)(a_{1,0}+a_{2,0})]\, k\,\Delta V \sin kx, \\ \gamma_2 &= -[A_t \tfrac{1}{2}(1+\tanh kh)(a_{1,0}-a_{2,0}) - A_c \tfrac{1}{2}(1+\coth kh)(a_{1,0}+a_{2,0})]\, k\,\Delta V \sin kx. \end{aligned}\right\} \tag{27}$$

For an initially varicose layer

$$\gamma_1 = \gamma_2 = -(1+\tanh kh)\, A_t k a_0 \Delta V \sin kx, \tag{28}$$

and for a sinuous layer

$$\gamma_1 = -\gamma_2 = -(1+\coth kh)\, A_c k a_0 \Delta V \sin kx, \tag{29}$$

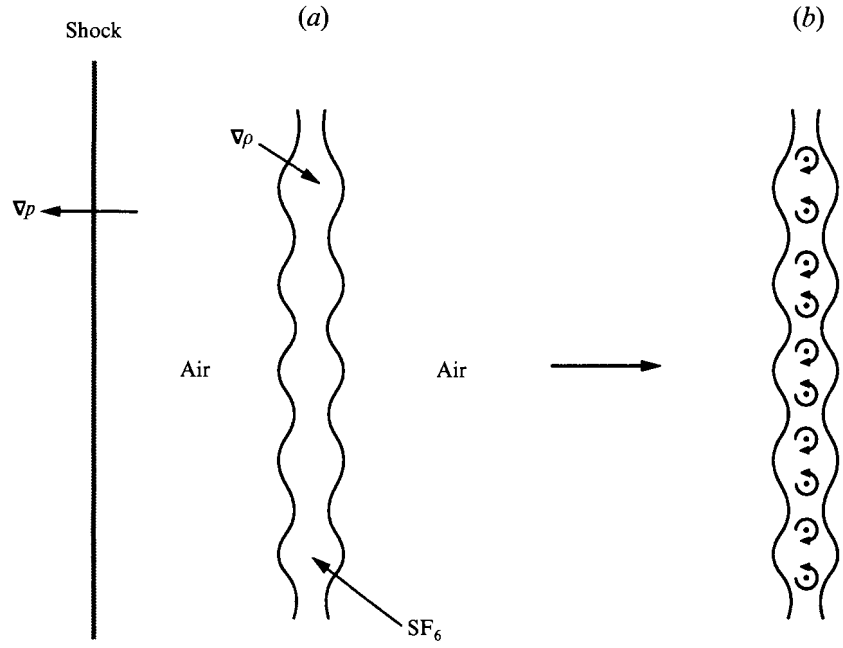

FIGURE 12. Vorticity is generated by the interaction of the pressure gradient from a shock wave with the density gradient at the boundary of the layer (*a*). The resulting vorticity distribution can be roughly approximated as a row of equally spaced vortices (*b*).

The jet technique used in our experiments generates a varicose layer with diffuse interfaces which cause the same sign vorticity on both sides of the layer to merge and become distributed throughout the layer. Thus, the result of the shock interaction is not to produce two sheets of vorticity, but a distribution more like a row of diffuse vortices with alternating sign, and spacing π/k (figure 12*b*). If it is then assumed that the vorticity contained in the vortex sheets is concentrated in a row of line vortices with strength $\pm K$, then

$$K = \frac{1}{2\pi}\int_0^{\pi/k} (\gamma_1 + \gamma_2)\,\mathrm{d}x = -\frac{1}{\pi}(1+\tanh kh)\,A_t\,\Delta V(a_{1,0} - a_{2,0}), \tag{30}$$

which for a varicose initial layer becomes

$$K = -\frac{2}{\pi}(1+\tanh kh)\,A_t\,\Delta V\,a_0. \tag{31}$$

Note that even if the interfaces are sharp, the vorticity on each boundary of a thin varicose layer will eventually roll up and combine to form a row of vortices each with strength roughly equal to that given by (31).

A row of line vortices will induce motion given by the stream function

$$\psi = \tfrac{1}{2}K\ln\left[\frac{\cosh(ky)+\sin(kx)}{\cosh(ky)-\sin(kx)}\right], \tag{32}$$

which will distort the layer. Near the vortex cores the induced velocity will act to wrap the layer around the vortices, but in the regions between the vortices the induced

motion works to push the layer in a direction perpendicular to the row. After a period of time, the spreading of the layer will be predominantly caused by the fluid motion near $x = 0, \pm\pi/k, \pm 2\pi/k, \ldots$. The velocity perpendicular to the vortex row is

$$v = -\frac{\partial \psi}{\partial x} = -kK\frac{\cosh(ky)\cos(kx)}{\cosh^2(ky) - \sin^2(kx)}, \tag{33}$$

which at $x = 0, \pm\pi/k, \pm 2\pi/k, \ldots$ reduces to

$$v = \frac{\mathrm{d}y}{\mathrm{d}t} = \pm\frac{kK}{\cosh(ky)}. \tag{34}$$

Because the horizontal component of velocity is zero at these points, (34) can be integrated directly to obtain

$$\left.\begin{aligned} y|_{x=0,\,\pm 2\pi/k,\,\ldots} &= (1/k)\sinh^{-1}[-k^2Kt + \sinh(ky_0)], \\ y|_{x=\pm\pi/k,\,\pm 3\pi/2k,\,\ldots} &= -(1/k)\sinh^{-1}[-k^2Kt + \sinh(ky_0)]. \end{aligned}\right\} \tag{35}$$

Equation (35) describes the displacement of the interface at the points $x = 0, \pm\pi/k, \pm 2\pi/k, \ldots$. The growth of the layer width is then given by

$$w = \frac{2}{k}\sinh^{-1}\left[\frac{2}{\pi}(1 + \tanh(\tfrac{1}{2}kw_0))\,k^2A_t\,\Delta V a_0\,t + \sinh(\tfrac{1}{2}kw_0)\right], \tag{36}$$

where w_0 is a measure of the average initial layer width. Note that for sufficiently large values of x, $\sinh^{-1}(x) \approx \ln(2x)$, therefore, according to this model, the late time growth of the layer is logarithmic in time. Also, for a sufficiently thick layer $\tanh(kw_0) \approx 1$, and $\sinh(kw_0) \approx \frac{1}{2}\exp(kw_0)$ so that

$$w = \frac{2}{k}\sinh^{-1}\left[\frac{4}{\pi}k^2A_t\,\Delta V a_0\,t + \tfrac{1}{2}\exp(\tfrac{1}{2}kw_0)\right], \tag{37}$$

and at large time

$$w \approx \frac{2}{k}\ln\left[\frac{8}{\pi}k^2A_t\,\Delta V a_0\,t + \exp(\tfrac{1}{2}kw_0)\right]. \tag{38}$$

Equation (36) was evaluated using known or measured values of k, A_t and ΔV ($k = 1.06\ \mathrm{mm}^{-1}$, $A_t = 0.74$, $\Delta V = 96\ \mathrm{m\ s}^{-1}$), and estimates of w_0 and a_0 ($w_0 = 2.6$ mm and $a_0 = 0.43$ mm). It is shown in figure 10 along with measurements of the layer width. Although there is a substantial amount of scatter in the measurements, the curve passes nearly through the middle of the data points. Furthermore the theory is in qualitative agreement with the measurements, showing a trend consistent with the data despite the scatter. Also plotted for reference in figure 10 is a line showing the growth in thickness of the layer if it were governed by linear instability theory. This curve was obtained using (23), noting that $w \approx w_0 + a_1 + a_2$, thus

$$w_{linear\,theory} = w_0 + 2kA_t\,\Delta V a_0\,t. \tag{39}$$

Note that linear theory greatly overestimates the layer thickness, especially at later times.

For a layer with a sinuous type of initial perturbation, the vortex sheet strengths given by (29) are equal and opposite. Thus, adding these strengths together and integrating, as is done in (30) to obtain the vortex strength, K, yields a vortex strength of zero. Consequently, it would appear that a sinuous perturbation produces no growth. However, even with diffuse boundaries, the opposite-signed vorticity on each

side of an initially sinuous layer will not combine to form a single row of vortices. It is, therefore, questionable whether our model applies to situations where $a_1(0)$ and $a_2(0)$ have the same sign. It can be argued that instead of forming a single row of vortices, the opposite-signed vorticity on each side of an initially sinuous layer will roll up independently, to form a distribution closer to that of a double row. If the spacing between these two rows is small (i.e. the layer is sufficiently thin), the motion induced by the opposite-signed vortices in this configuration would tend counteract each other, and impede growth. Therefore, even though our model may not strictly apply to situations where the vorticity on opposite sides of the layer differ in sign, it may provide a good approximation to what actually occurs in a sufficiently thin layer. Because we have not performed experiments in which opposite-signed vorticity is generated, we can only speculate about this outcome. However, this conjecture is in agreement with numerical results of Mikaelian (1993), who observed that the instability of a thin sinuous layer is one of very slow growth.

The row of equidistant vortices used to model the flow generated from the layer with varicose initial shape is well known to be unstable. Note that this vorticity distribution is identical to that of a vortex street with zero width, the stability of which was analyzed by von Kármán (see Lamb 1945, p. 225, and references cited therein to von Kármán's studies). One mode of instability can be generated by uniformly displacing every other vortex along the row, producing a row of vortex pairs, which will cause the entire row of vortices to move in a direction perpendicular to the layer. Thus, small perturbations to the initial distribution of vortices in our experiments can generate vortex pairs (or mushrooms) which travel upstream or downstream. The type of mushroom (upstream or downstream) would then be determined by whether the vortex pairing occurs at the thick or thin parts of the layer. Because the initial distribution of vorticity is not discrete, but is in reality distributed regions of vorticity, a nearly uniform vortex spacing will cause the distributed vortex cores to be strained by the induced flow field. This stretching will act to pull apart the vortex cores, thus inhibiting roll-up and producing what we observe as the sinuous mode.

5. Conclusions

We have experimentally discovered the apparent bifurcation of a shock-accelerated thin gas layer by observing three randomly occurring but reproducible flow patterns. Two of these are distinguished by the appearance of upstream- or downstream-moving vortex pairs while the third is a sinuous pattern which shows no vortex formation until late in the evolution. We believe that the patterns are the result of an instability which is sensitive to the shape of the initial layer. Experimental techniques that facilitated this discovery are: (i) the use of a planar gas jet to produce membrane-free interfaces, and (ii) PLIF imaging to observe a cross-section of the flow without the obscuring effects of boundary disturbances. Multiframe imaging (unavailable for our experiments) is needed to determine the precise sensitivity to the initial conditions. (Budzinski, Benjamin & Jacobs 1994).

We interpret this phenomenon using an analytical model based on the assumption that the vorticity created by the initial shock interaction evolves into a row of line vortices. The model uses linear stability theory to predict the strength of the vortices which then displace the layer profile by their induced motion. The model predicts that the layer thickness grows logarithmically in time at late times and compares well with our measurements of the growth of the layer thickness. Because perturbing the location of the vortices in the vortex row produces vortex pairs (observed as mushroom

patterns) which move upstream or downstream in the shock-tube flow, the vortex model also provides an explanation for our observations of the three instability patterns.

This research has been supported by US Department of Energy Contract No. W-7405-ENG-36. We are grateful to R. Reinovsky and J. Shaner for advice and encouragement, to R. Haight for use of the camera, to C. Findley and D. Bannerman for technical assistance, and to J. Budzinski, J.-M. Le Peuvedic for assistance in interpreting data and calculations. We are also grateful to referee B for stimulating communication that helped us clarify the mechanisms of circulation deposition.

REFERENCES

ANDRONOV, V. A., BAKHRAKH, S. M., MESHKOV, E. E., MOKHOV, V. N., NIKIFOROV, V. V., PEVNITSKII, A. V. & TOLSHMYAKOV, A. I. 1976 Turbulent mixing at contact surface accelerated by shock waves. *Sov. Phys. JETP* **44**, 424–427. (Russian: *Zh. Eksp. Teor. Fiz.* **71**, 806, August 1976.)

ANDRONOV, V. A., BAKHRAKH, S. M., MESHKOV, E. E., NIKIFOROV, V. V., PEVNITSKII, A. V. & TOLSHMYAKOV, A. I. 1983 An experimental investigation and numerical modeling of turbulent mixing in one-dimensional flows *Sov. Phys. Dokl.* **27**, 393–396. (Russian: *Dokl. Akad. Nauk SSSR* **264** (1), 76, 1982.)

BENJAMIN, R. F. 1988 Experimental observations of shock stability and shock-induced turbulence. In *Proc. First Intl Workshop on the Physics of Compressible Turbulent Mixing, Princeton* (ed. W. P. Dannevick, A. C. Buckingham & C. E. Leith). Lawrence Livermore Lab. Rep. CONF-8810234 (January 1992).

BENJAMIN, R. F., BESNARD, D. C. & HAAS, J. F. 1993 Shock and reshock of an unstable fluid interface *Los Alamos Rep.* LA-UR 92-1185 (1993). (*Phys. Fluids*, submitted.)

BENJAMIN, R. F. & FRITZ, J. N. 1987 Shock loading a rippled interface between liquids of different densities. *Phys. Fluids* **30**, 331.

BONAZZA, R. 1992 X-ray measurements of shock-induced mixing at an air/xenon interface. PhD thesis, California Institute of Technology.

BROUILLETTE, M. 1989 On the interaction of shock waves with contact surfaces between gases of different densities. PhD thesis, California Institute of Technology.

BUDZINSKI, J. M. 1992 Planar Rayleigh scattering measurements of shock enhanced mixing. PhD thesis, California Institute of Technology. Budzinski, J. M., Zukoski, E. E. & Marble, F. E. 1992 *Proc. 28th Joint Propulsion Conference and Exhibit, Rayleigh Scattering Measurements of Shock Enhanced Mixing, July 6–8, 1992, Nashville TN, AIAA 92-3546.*

BUDZINSKI, J. M., BENJAMIN, R. F. & JACOBS, J. W. 1994 Influence of initial conditions on the flow patterns of a shock-accelerated thin fluid layer. *Phys. Fluids* **6**, 3510–3512.

CAVAILLER, C., MERCIER, P., RODRIGUEZ, G. & HAAS, J. F. 1990 A new vertical shock tube for Rayleigh–Taylor instability measurements, *Proc. 17the ISSWST at Bethlehem PA, Current Topics in Shock Waves* (ed. Y. Kim) p. 564.

EPSTEIN, A. H. 1974 Fluorescent gaseous tracers for three dimensional flow visualization. *MIT Gas Turbine Lab Rep.* 117 (unpublished).

GLIMM, J., SHARP, D. H. & ZHANG, Q. 1991 The renormalization group dynamics of chaotic mixing of unstable interfaces. *Phys. Fluids* A **3**, 1333–1335.

HAWLEY, J. F. & ZABUSKY, N. J. 1989 Vortex paradigm for shock-accelerated density-stratified interfaces. *Phys. Rev. Lett.* **63**, 1.

JACOBS, J. W. 1992 Shock-induced mixing of a light-gas cylinder. *J. Fluid Mech.* **234**, 629–649.

JACOBS, J. W. 1993 The dynamics of shock accelerated light and heavy gas cylinders. *Phys. Fluids* A **5**, 2239–2247.

JACOBS, J. W., KLEIN, D. L., JENKINS, D. G. & BENJAMIN, R. F. 1993 Instability growth patterns of a shock-accelerated thin fluid layer. *Phys. Rev. Lett.* **70**, 583–586.

LAMB, H. 1945 *Hydrodynamics*. Dover.

LEWIS, D. J. 1950 The instability of liquid surfaces when accelerated in a direction perpendicular to their planes. II. *Proc. R. Soc. Lond.* A, **202**, 81–96.

MCCALL, G. H. 1983 Laser-driven implosion experiments. *Plasm Phys.* **25**, 237–285.

MESHKOV, E. E. 1969 Instability of the interface of two gases accelerated by a shock wave. *Izv. Akad. Nauk. SSSR Mekh. Zhidk. Gaza* **4**, 151–157. (Russian: *Izv. Acad. Sci. USSR Fluid Dyn.* **4**, 101–104.)

MIKAELIAN, K. O. 1990 Rayleigh–Taylor and Richtmyer–Meshkov instabilities in multilayer fluids with surface tension. *Phys. Rev.* A **42**, 7211–7225.

MIKAELIAN, K. O. 1993 Rayleigh–Taylor and Richtmyer–Meshkov instabilities in finite-thickness fluid layers. *Lawrence Livermore National Laboratory Rep.* UCRL-JC-114338.

PCTM WORKSHOPS, 1988–1993: *Proc. First Intl Workshop on the Physics of Compressible Turbulent Mixing, Princeton, October 1988* (ed. W. P. Dannevik, A. C. Buckingham & C. E. Leith), Lawrence Livermore Laboratory Rep No. CONF-8810234 (January 1992); *Proc. Second Intl Workshop on the Physics of Compressible Turbulent Mixing, Pleasanton CA, 1989* (compiled by V. Rupert), available from Lawrence Livermore National Laboratory; *Proc. Third Intl Workshop on the Physics of Compressible Turbulent Mixing, Abbey of Royaumont, France, 17–19 June 1991*, Commissariat a l'Engergie Atomique (CEA) report; *Proc. Fourth Intl Workshop on the Physics of Compressible Turbulent Mixing, Cambridge, England, March–April 1993*, to be published.

PICONE, J. M. & BORIS, J. P. 1988 Vorticity generation by shock propagation through bubbles in a gas. *J. Fluid Mech.* **189**, 23–51.

RAYLEIGH, LORD 1883 Investigation of the character of the equilibrium of an incompressible heavy fluid of variable density. *Proc. Lond. Math. Soc.* **14**, 170–177. (Reprinted in *The Scientific Papers of Lord Rayleigh*, vol. II, p. 200. Cambridge University Press, 1900.)

RICHTMYER, R. D. 1960 Taylor instability in shock acceleration of compressible fluids. *Commun. Pure Appl. Maths* **23**, 297–319.

SHANER, J. W. 1984 Pattern formation by shock processes. *Physica* D **12**, 154–162.

SHARP, D. H. 1984 An overview of Rayleigh–Taylor instability. *Physica* D **12**, 3–18.

TAYLOR, G. I. 1950 The instability of liquid surfaces when accelerated in a direction perpendicular to their planes. I. *Proc. R. Soc. Lond.* A **201**, 192–196.

YANG, X., ZABUSKY, N. J. & CHERN, I.-L. 1990 'Breakthrough' via dipolar-vortex/jet formation in shock-accelerated density-stratified layers. *Phys. Fluids* A **2**, 892–895.

YANG, Y., ZHANG, Q. & SHARP, D. H. 1993 Small amplitude theory of Richtmyer–Meshkov instability. *Phys. Fluids* **6**, 1856–1873.

YOUNGS, D. L. 1984 Numerical simulation of turbulent mixing by Rayleigh–Taylor instability. *Physica* D **12**, 32–44.